Research Article

René Sachse, Vasile-Dan Hodoroaba, Ralph Kraehnert and Andreas Hertwig*

# Multilevel effective material approximation for modeling ellipsometric measurements on complex porous thin films

https://doi.org/10.1515/aot-2022-0007
Received March 15, 2022; accepted May 17, 2022;
published online June 22, 2022

**Abstract:** Catalysts are important components in chemical processes because they lower the activation energy and thus determine the rate, efficiency and selectivity of a chemical reaction. This property plays an important role in many of today's processes, including the electrochemical splitting of water. Due to the continuous development of catalyst materials, they are becoming more complex, which makes a reliable evaluation of physicochemical properties challenging even for modern analytical measurement techniques and industrial manufacturing. We present a fast, vacuum-free and non-destructive analytical approach using multi-sample spectroscopic ellipsometry to determine relevant material parameters such as film thickness, porosity and composition of mesoporous $IrO_x$–$TiO_y$ films. Mesoporous $IrO_x$–$TiO_y$ films were deposited on Si wafers by sol–gel synthesis, varying the composition of the mixed oxide films between 0 and 100 $wt\%_{Ir}$. The ellipsometric modeling is based on an anisotropic Bruggeman effective medium approximation (a-BEMA) to determine the film thickness and volume fraction of the material and pores. The volume fraction of the material was again modeled using a Bruggeman EMA to determine the chemical composition of the materials. The ellipsometric fitting results were compared with complementary methods, such as scanning electron microscopy (SEM), electron probe microanalysis (EPMA) as well as environmental ellipsometric porosimetry (EEP).

**Keywords:** electrochemical catalysts; mixed metal oxide; multi-sample analysis; spectroscopic ellipsometry; thin mesoporous films.

## 1 Introduction

Catalysis plays an important role in technical chemistry for the production of chemicals, novel products or pharmaceuticals. Catalysis also plays a crucial role in energy conversion processes, as catalysts determine the rate, efficiency and selectivity of electrochemical reactions. Electrochemical conversion processes for large-scale hydrogen production can contribute to the efficiency of energy transformation. However, the current state of the art still relies on expensive and rare precious metals such as platinum or iridium. Therefore, a more efficient use of catalyst materials requires a reduction in the current precious metal content.

The introduction of supported nanoparticles or porous coatings are promising approaches to reduce the noble metal content while maintaining the activity. In this context, both nanoparticles and porous coatings have a high surface-to-volume ratio and thus serve to increase the active surface area. The latter represents a good compromise between surface chemical catalysis and mass transfer.

Iridium oxide-based catalysts are typically used for the oxygen evolution reaction (OER) in the electrochemical water splitting, as they exhibit a good combination of both activity and stability. Yet, iridium and its oxides are scarce and expensive resources and therefore require an efficient use. This can be achieved by increasing the active surface area through the synthesis of nanoparticles or the introduction of porosity. In the case of porous materials, studies show that the introduction of porosity in such materials leads to a significant reduction in the required overpotential [1]. A mesoporous $IrO_x$ film thus shows a reduction in overpotential of about 17% compared to the non-porous catalyst film [2].

***Corresponding author: Andreas Hertwig**, Federal Institute for Materials Research and Testing (BAM), Unter den Eichen 44-46, 12203 Berlin, Germany, E-mail: andreas.hertwig@bam.de. https://orcid.org/0000-0002-1380-0109
**René Sachse and Vasile-Dan Hodoroaba,** Federal Institute for Materials Research and Testing (BAM), Unter den Eichen 44-46, 12203 Berlin, Germany, E-mail: rene.sachse@bam.de (R. Sachse). https://orcid.org/0000-0002-3611-3352 (R. Sachse). https://orcid.org/0000-0002-7901-6114 (V.-D. Hodoroaba)
**Ralph Kraehnert,** Technische Universität Berlin, Straße des 17. Juni 135, 10623 Berlin, Germany. https://orcid.org/0000-0002-6159-9585

Another way to reduce cost is to replace the expensive noble metals with less costly materials. Current research is mainly focused on metal oxides such as $MnO_x$, $FeO_x$, $CoO_x$ and $NiO_x$ due to their good activity in the OER under acidic conditions [3]. In this context, $MnO_x$ seems to be a very attractive candidate since it is a very stable material in low pH electrolytes [4]. However, a major drawback of these materials is usually the higher overpotential required, which reduces the efficiency of catalysis.

An alternative approach is to add a second element or material to either increase the activity by changing the structure or to reduce the precious metal content while maintaining the activity. Willinger et al. showed in their work that adding potassium to the iridium oxide catalyst can change the crystal structure, thus leading to an increase in activity [5]. Oakton et al., on the other hand, pursued the approach of dispersing iridium oxide nanoparticles in titanium oxide in their studies and were thus able to achieve a reduction in the noble metal content [6, 7]. A similar approach to the latter was also followed by Bernicke et al. in which they synthesized a mesoporous network of iridium oxide and titanium oxide [8, 9]. These synthesized mixed oxide films showed high conductivity and high surface area and activity in the acidic OER.

These studies show that the catalyst materials developed today are becoming increasingly complex, making reliable evaluation of physicochemical properties challenging even for modern analytical measurement techniques. Many characterization procedures are performed in high vacuum and are not always completely non-destructive, especially when parameters such as layer thickness or the chemical composition are to be determined. For instance, the reductive electron beam used in electron microscopy (EM) can alter material properties. Also, transmission electron microscopy (TEM) studies have shown that the electron beam is able to reduce $IrO_x$ to Ir and thus misinterpretation of the results may occur [10]. Other methods such as X-ray photoelectron spectroscopy (XPS) or secondary ion mass spectrometry (SIMS) to determine the chemical composition of the material at the outer surface and below (in the bulk) also involve the destruction of the material (e.g., by sputtering). As an alternative to these techniques, spectroscopic ellipsometry can serve as a vacuum-free and non-destructive method. It involves determining changes in the polarization state of an electromagnetic wave upon reflection, resulting in a change in amplitude ratio and a phase shift [11, 12].

The group around Sanchez showed in their work ellipsometric investigations of the porosity and pore sizes of a bimetallic mesoporous $NbVO_5$ film [13]. May et al. also showed ellipsometric studies of mixed $MoWO_x$ films in their study and determined the band gap energy as a function of Mo content [14]. Here, the authors used for each $MoWO_x$ film a separate model. Buiu et al. also focused on ellipsometric studies of mixed metal oxides and showed a dependence of the band gap energy on the composition of hafnium silicate films [15]. Also in this case, the different compositions were modeled with a separate model, which means that no information about the composition of the films can be obtained.

Here we report on the vacuum-free and non-destructive ellipsometric analysis and modeling of bimetallic mesoporous $IrO_x$–$TiO_y$ films with different weight percent (0–100 $wt\%_{Ir}$) Ir in $Ir/TiO_2$ to determine relevant parameters like film thickness, porosity and chemical composition, using only the models of the pure metal oxides (i.e., $IrO_x$ and $TiO_y$). This approach includes the characterization and modeling of the pure mesoporous $IrO_x$ and $TiO_y$ films with an anisotropic Bruggeman effective medium approximation (a-BEMA). The variations of the bimetallic mesoporous $IrO_x$–$TiO_y$ films were then characterized using the pure metal oxide models in a Bruggeman effective medium approximation (BEMA) with a multi-sample analysis (MSA). The derived material parameters such as film thickness, porosity and their chemical composition were validated by complementary methods such as scanning electron microscopy (SEM), electron probe microanalysis (EPMA) and environmental ellipsometric porosimetry (EEP).

# 2 Experimental

## 2.1 Chemicals

Iridium acetate ($Ir[CH_3COO]_n$, 99.95% metal base, about 48% Ir) from chemPUR and titanium chloride ($TiCl_4$, 99.9%) from Sigma-Aldrich were used to synthesize the mesoporous iridium–titania films. The polymer template (PEO-PB-PEO, containing 18,700 g $mol^{-1}$ polyethylene oxide [PEO] and 10,000 g $mol^{-1}$ polybutadiene [PB]) was purchased from Polymer Service Merseburg GmbH [16]. Ethanol (EtOH, >99%) was used as solvent from Sigma-Aldrich. All chemicals were used without further preparation. The films were deposited on unilaterally polished Si wafers with (100)-orientation (Siegert wafers) via dip coating under controlled conditions (see Synthesis). The Si wafers were cleaned with ethanol prior to film deposition. For quantification and validation of Ir mass loading, an iridium foil (0.25 mm thick, 99.8% [metal base], 22.7 g $cm^{-3}$; abcr chemicals GmbH), a $TiO_2$ reference material, and a Si wafer from Siegert Wafers were used as reference materials for electron probe microanalysis (EPMA).

## 2.2 Synthesis of iridium-titanium oxide films

Iridium titanium oxide films were prepared in a slightly modified synthesis to that described by Bernicke et al. [8] In a typical synthesis

for a 30 wt% $IrO_x$–$TiO_y$ film (30 wt% Ir in $Ir/TiO_2$), 141 mg of the PEO-PB-PEO polymer template was dissolved in 3.75 ml ethanol at 40 °C. After complete dissolution, a second solution containing 751 mg of titanium(IV) chloride in 3.75 ml of ethanol was added and mixed at 40 °C for 1 h. Subsequently, 272 mg of iridium(III) acetate was added and mixed at 40 °C for another hour. The dark green solution obtained was transferred to a preheated Teflon cuvette (40 °C) and immediately coated by immersion under controlled conditions (25 °C, 40% relative humidity) at a withdrawal rate of 200 mm $min^{-1}$. The films thus prepared were dried under the same conditions for 5 min and then calcined in a preheated muffle furnace in flowing air at 400 °C for 10 min. For the variation of $wt\%_{Ir}$ within the $IrO_x$–$TiO_y$ films was realized by adjusting the amount of iridium(III) acetate during the synthesis.

## 2.3 Physicochemical characterization

Ellipsometry measurements were performed using a variable angle M2000 DI spectroscopic ellipsometer (J.A. Woollam) in a spectral range between 192 and 1697 nm. The spectral resolution of the used ellipsometer is about 5 nm bandwidth in the UV/Vis and about 10 nm in the NIR. The mesoporous $IrO_x$–$TiO_y$ films on single polished (100) silicon substrates were measured at angles of incidence (AOI) of 55°, 60°, 65°, 70°, and 75° relative to the normal. The measured Ψ and Δ spectra were modeled using CompleteEASE software (v6.42). The pure $IrO_x$ and $TiO_y$ films were modeled, respectively, and the $IrO_x$–$TiO_y$ mixed oxide films were subsequently analyzed with the models of the pure films in a multi-sample analysis with respect to their film thickness, porosity, and composition.

The porosities of the films were additionally analyzed using environmental ellipsometric porosimetry (EEP) with an ambient cell and a fixed incidence angle of 60°. Pure water served as the solvent. Relative humidity was adjusted by mixing a water-saturated nitrogen gas flow with a dry nitrogen gas flow. The total $N_2$ flow was 2 l $min^{-1}$, controlled by two mass flow controllers, at a constant temperature of 23 °C. Relative humidity was measured for the exiting gas flow and for each water partial pressure downstream of the cell.

Scanning electron microscope (SEM) images were acquired on a JEOL 7401F at 10 kV. Images were then analyzed for extracting the film thickness using the ImageJ program (v. 1.51w, www.imagej.nih.gov/ij/). EPMA were performed on a Carl Zeiss Supra 40 equipped with a Schottky field emitter and an energy dispersive X-ray spectrometer (EDS) with a 10 $mm^2$ silicon drift detector (SDD) having an energy resolution of 123 eV (Bruker XFlash 5010). Here, the measured net peak X-ray intensities of interest were divided by the electron probe current and spectra lifetime to calculate the $k_{EPMA}$ values. EDS spectra were recorded at accelerating voltages of 15, 20, 25, and 30 kV for the Ir $L_\alpha$, Ti $K_\alpha$, O $K_\alpha$, and Si $K_\alpha$ lines, respectively. StrataGem thin-film analysis software (v. 6.7 SAMx, Guyancourt, France) was used for quantification of the chemical composition [17].

## 2.4 Ellipsometric modeling

Mesoporous metal oxide films were generally modeled using an anisotropic Bruggeman effective medium approximation (a-BEMA) described by D. Schmidt and M. Schubert, due to the synthesis-related ellipsoidal pore geometries in the *z*-direction, i.e., perpendicular to the substrate [18].

The (a-BEMA) is expressed as follows:

$$\sum_i f_i \frac{\epsilon_i - \epsilon_{\mathrm{eff,j}}}{\epsilon_{\mathrm{eff,j}} + L_j(\epsilon_i - \epsilon_{\mathrm{eff,j}})} = 0 \tag{1}$$

with depolarization factors:

$$L_j = \frac{U_x U_y U_z}{2} \int_0^\infty \frac{\left(s + U_j^2\right)^{-1} \mathrm{ds}}{\sqrt{\left(s + U_x^2\right)\left(s + U_y^2\right)\left(s + U_z^2\right)}} \tag{2}$$

$\epsilon_i$ as dielectric functions and $f_i$ as volume fraction of the $i^{th}$ component (i.e., the guest fraction, $i = a, b, c$), and $\epsilon_{\mathrm{eff,j}}$ describes the effective major dielectric function ($j$ = x, y, z) [18]. The real depolarization factors $L_j$ only depend on the real shape parameters $U_j$ of the ellipsoid and the two relationships ($U_x/U_z$) and ($U_y/U_z$) serve to precisely define the shape [18].

In this context, the a-BEMA layer consists of the volume fraction of the metal oxide matrix and void. In the case of the bimetallic mixed oxides, the metal oxide matrix was modeled using a BEMA to model the volume fractions of both metal oxide matrix materials.

The BEMA is defined as:

$$0 = \sum_i f_i \frac{\epsilon_i - \epsilon_{\mathrm{EMA}}}{\epsilon_i + \gamma \epsilon_{\mathrm{EMA}}} \tag{3}$$

with $\epsilon_{\mathrm{EMA}}$ as dielectric constant of the mixed phase, $\epsilon_i$ as dielectric functions and $f_i$ as volume fraction of the $i^{th}$ component (i.e., the guest fraction, $i$ = a, b, c) [12, 19]. $\gamma$ represents the factor that describes the shape of the guest volume and can be expressed as follows:

$$\gamma = \frac{1}{L} - 1 \tag{4}$$

where $L$ defined the depolarization factor. In the isotropic case, i.e., for 3-dimensional spheres, $L = 1/3$ and $\gamma = 2$ [19].

The titanium oxide matrix material was modeled by a summation of two coupled Tauc-Lorentz functions to describe the optical properties of amorphous semiconductors near the band edge [20]. The Tauc–Lorentz function described in detail by G. E. Jellison Jr. and F. A. Modine and is expressed as follows [21, 22]:

$$\epsilon_{\mathrm{T\text{–}L_n}}(E) = \frac{\mathrm{Amp_n En_n \Gamma_n}\left(E - E_g\right)^2}{\left(E^2 - \mathrm{En_n^2}\right) + \Gamma_n^2 E^2} \cdot \frac{1}{E}; \quad E \geq E_g \tag{5}$$

$$\epsilon_{\mathrm{T\text{–}L_n}}(E) = 0; \quad E \leq E_g \tag{6}$$

where $\mathrm{Amp_n}$ is the amplitude of the $n^{th}$ oscillator (eV), $\mathrm{En_n}$ the center energy of $n^{th}$ oscillator (eV), $\Gamma_n$ the width (full width at half-maximum) of the $n^{th}$ oscillator (eV) and $E_g$ the band-gap energy (eV). Fit parameters of the Tauc–Lorentz parametrization are the amplitude $\mathrm{Amp_n}$, the width $\Gamma_n$, the center energy $\mathrm{En_n}$, and the band-gap energy $E_g$.

The iridium oxide matrix material was modeled with a multi-peak function model using a Drude function to describe free carrier effects [23, 24], due to the electrical conductivity of the $IrO_x$ material and three Lorentz functions for the description of different atomic transitions [11, 19].

The Drude functions is defined as:

$$\epsilon_{\mathrm{Drude}}(E) = \frac{-\hbar^2}{\epsilon_0 \rho_R \left(\tau E^2 + i\hbar E\right)} \tag{7}$$

with

$$\rho_R = \frac{m^*}{N q^2 \tau} = \frac{1}{q \mu N} \tag{8}$$

where $E$ is the photon energy ($E = h\nu = \hbar\omega$), $\hbar$ the reduced Planck constant, $\epsilon_0$ the vacuum dielectric constant, $\rho_R$ the resistivity (Ω cm),

$\tau$ the mean scattering time (fs), $m^*$ the electron effective mass ($9.11 \cdot 10^{-31}$ kg), $N$ the electron concentration ($cm^{-3}$), $q$ the electron charge ($1.60 \cdot 10^{-19}$ C) and $\mu$ the electron mobility ($cm^2\ V^{-1}\ s^{-1}$) [25]. Fit parameters for the Drude model are the resistivity $\rho_R$ and the mean scattering time $\tau$.

The Lorentz function is defined as:

$$\epsilon_{\mathrm{Lorentz_n}}(E) = \frac{\mathrm{Amp_n}\Gamma_n \mathrm{En_n}}{\mathrm{En_n^2} - E^2 - iE\Gamma_n} \tag{9}$$

with $\mathrm{Amp_n}$ as the amplitude of the $n^{\mathrm{th}}$ oscillator (unitless), $\Gamma_n$ width (full width at half-maximum) of the $n^{\mathrm{th}}$ oscillator (eV) and $\mathrm{En_n}$ the center energy of $n^{\mathrm{th}}$ oscillator (eV) [26]. The fit parameters of the Lorentz parametrization are the amplitude $\mathrm{Amp_n}$, the width $\Gamma_n$ and the center energy $\mathrm{En_n}$.

### 2.5 Root mean squared deviation

In order to minimize the deviation between theoretical and experimental measured variables, the definition of a figure of merit, the root mean squared deviation ($D_{\mathrm{RMS}}$), was used. The $D_{\mathrm{RMS}}$ can be expressed as follows:

$$D_{\mathrm{RMS}} = \sqrt{\frac{1}{3Y - Z}\sum_{i=1}^{Y}\left[\left(\frac{N_i^{\mathrm{fit}} - N_i^{\mathrm{exp}}}{0.001}\right)^2 + \left(\frac{C_i^{\mathrm{fit}} - C_i^{\mathrm{exp}}}{0.001}\right)^2 + \left(\frac{S_i^{\mathrm{fit}} - S_i^{\mathrm{exp}}}{0.001}\right)^2\right]} \tag{10}$$

with

$$N = \cos(2\Psi) \tag{11}$$
$$C = \sin(2\Psi)\cos(\Delta) \tag{12}$$
$$S = \sin(2\Psi)\sin(\Delta) \tag{13}$$

where $Y$ is the number of wavelengths and $Z$ the number of fit parameters.

### 2.6 Multi-sample-analysis

Measuring multiple samples of the same material with different properties, such as film thickness, is mostly used to gain additional information about the dielectric function and reduce the correlation between model functions and material parameters. However, multi-sample analysis can also be used to investigate the properties of several samples simultaneously [27]. However, for this purpose, the following sample properties must be assumed:

(1) All samples are of the same type, i.e., they are mesoporous metal oxide films with a comparable porosity, deposited on the same Si substrates with a native oxide layer and calcined at the same temperature.
(2) We assumed that the matrix material properties of the pure metal oxides ($IrO_x$, $TiO_y$) are unchanged for the mixed oxides with different compositions.
(3) The models of the pure metal oxides, i.e., the $TiO_y$ model and the $IrO_x$ model, are used for modeling the matrix material of the mixed oxides.
(4) For the modeling of the mixed oxides only the thickness, porosity, composition and pore geometry in $z$-direction were varied.
(5) No surface roughness layers or other special considerations, such as a material gradient, were assumed for the modeling.

## 3 Results and discussion

Mesoporous $IrO_x$–$TiO_y$ films are complex due to their porosity and the mixture of two materials and cannot be analyzed directly ellipsometrically with MSA since parameter couplings may occur. Therefore, in a first step, the individual components of the mixtures, i.e., $IrO_x$ and $TiO_y$, are analyzed separately to determine the dielectric functions of the materials. Then, the analysis of the mixed phases, which were varied between 0 and 100 wt% Ir-content ($wt\%_{Ir}$), is performed using the previously determined dielectric functions of the pure metal oxides to determine the film thickness, porosity and chemical composition. These parameters were determined by the MSA, which were additionally validated by independent methods for the accuracy of the result.

Table 1 gives an overview of the spectroscopic ellipsometry results for the pure mesoporous metal oxide films and for the mesoporous mixed metal oxide films. The second section of Table 1 summarizes the results of the complementary methods for film thickness, porosity and Ir-content.

### 3.1 Mesoporous $TiO_y$ film

The mesoporous $TiO_y$ film was synthesized in a slightly different synthesis than described in the literature [16, 27–29], deposited on a Si substrate via dip coating and calcined in a preheated muffle furnace at 400 °C under air for 20 min. SEM images in Figure 1a and b show a uniform pore surface and film thickness of the synthesized films.

For the modeling of the ellipsometry spectra, a model consisting of a Si substrate (literature values) [30, 31], a native oxide layer (literature values) [32] and a-BEMA [18] layer (Eq. (1)) was used. The a-BEMA layer is composed of the volume of the $TiO_y$ material (two $E_g$ coupled Tauc–Lorentz [Eqs. (5) and (6)]) and the pore volume (void). By removing the template polymer during calcination, the layer shrinks, and the pores acquire an elliptical shape. This is fitted by the anisotropy factor in $z$-direction of the a-BEMA layer.

Figure 2 shows the measured and modeled $\Psi$ and $\Delta$ spectra (AOI: 55–75°, in 5° steps), as well as the dielectric functions.

Both the modeled $\Psi$ and $\Delta$ spectra show good agreement with the measured values, whereas some larger deviations between model and measured $\Delta$ spectra are observed in the region around 4–5 eV (Figure 2a and b). However, the $D_{\mathrm{RMS}}$ value does not exceed 22.408. Figure 2c

**Table 1:** Summary of material properties of mesoporous $IrO_x$–$TiO_y$ films derived from spectroscopic ellipsometry and material properties of the complementary methods.

| Method | Property | 0 wt%$_{Ir}$ | 15 wt%$_{Ir}$ | 30 wt%$_{Ir}$ | 45 wt%$_{Ir}$ | 60 wt%$_{Ir}$ | 75 wt%$_{Ir}$ | 100 wt%$_{Ir}$ |
|---|---|---|---|---|---|---|---|---|
| | Spectroscopic ellipsometric measurements and modeling | | | | | | | |
| Spectroscopic ellipsometry | Thickness / nm | 133.1 ± 1.7 | 141.9 ± 2.3 | 135.1 ± 2.3 | 150.9 ± 2.3 | 111.8 ± 2.3 | 73.2 ± 2.3 | 60.6 ± 2.3 |
| | Porosity / % | 46.8 ± 0.9 | 41.6 ± 1.2 | 43.5 ± 1.2 | 50.0 ± 1.6 | 50.0 ± 2.0 | 42.6 ± 2.5 | 44.3 ± 2.5 |
| | Ir-content / vol% | 0.0 ± 2.9 | 7.2 ± 2.7 | 14.8 ± 2.9 | 24.3 ± 3.5 | 42.7 ± 6.1 | 63.3 ± 9.1 | 100.0 ± 7.5 |
| | Ir-content / wt% | 0.0 ± 2.9 | 15.4 ± 2.7 | 29.0 ± 2.9 | 43.0 ± 3.5 | 63.1 ± 6.1 | 80.2 ± 9.1 | 100.0 ± 7.5 |
| | Single $D_{RMS}$ | 22.408 | 51.982 | 48.161 | 71.488 | 38.476 | 34.421 | 8.274 |
| | MSA $D_{RMS}$ | | | | 44.922 | | | |
| | Measurements and results of complementary methods | | | | | | | |
| Ellipsometric porosimetry | Porosity / % | 48.7 ± 1.2 | 46.8 ± 1.2 | 47.1 ± 1.2 | 49.5 ± 1.2 | 53.1 ± 1.2 | 46.9 ± 1.2 | 41.8 ± 1.2 |
| | $D_{RMS}$ | 20.844 | 52.514 | 46.865 | 73.855 | 26.953 | 42.252 | 4.354 |
| SEM/EPMA | Thickness / nm | 130.7 ± 4.9 | 152.5 ± 2.2 | 135.7 ± 10.4 | 131.2 ± 6.3 | 101.4 ± 2.5 | 67.0 ± 4.6 | 74.4 ± 1.8 |
| | Ir-content / wt% | 0.0 ± 0.0 | 13.1 ± 7.0 | 29.8 ± 4.7 | 44.8 ± 7.1 | 57.1 ± 5.5 | 66.5 ± 12.0 | 100.0 ± 0.0 |

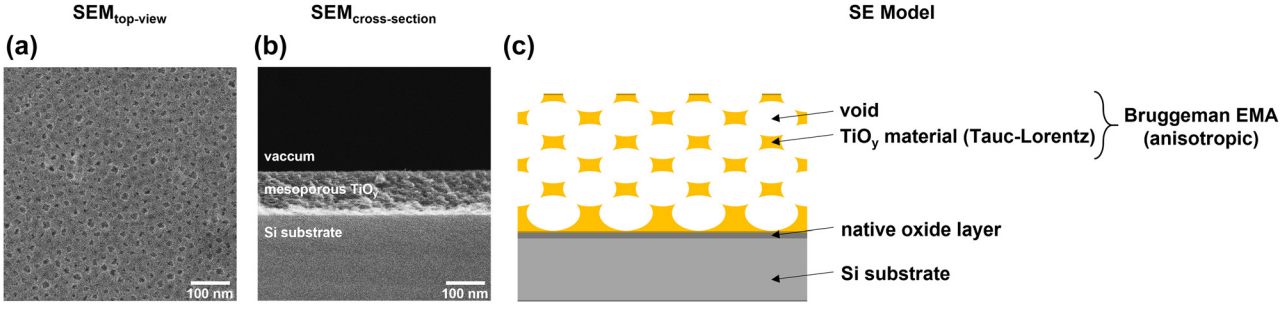


**Figure 1:** Characterization and modeling approach of a mesoporous $TiO_y$ film calcined at 400 °C for 20 min in air. (a) SEM top-view image indicating a mesoporous network at the outer surface area. (b) Cross-sectional SEM images show a uniform film thickness of about 130 nm. (c) Illustration of the used model for spectroscopic ellipsometry.

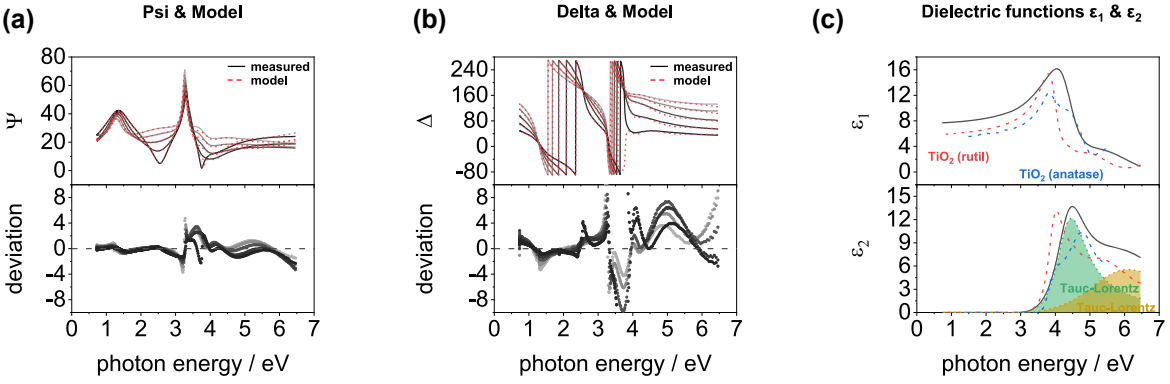


**Figure 2:** Measured and modeled Ψ (a) and Δ (b) spectra using AOI's between 55 and 75° (in 5° steps) as well as the deviation between measured and modeled Ψ and Δ spectra. (c) Real ($\varepsilon_1$) and imaginary ($\varepsilon_2$) parts of the dielectric function of the mesoporous $TiO_y$ film calcined at 400 °C.

shows the dielectric function of $TiO_y$ material described by two coupled Tauc–Lorentz functions. For comparison, literature values of the ordinary dielectric functions of the rutile [33] and anatase [34] phases of $TiO_2$ are shown. The dielectric functions of the mesoporous $TiO_y$ layer are more similar in shape to the $TiO_2$ rutile phase than the anatase phase. In both spectra ($\varepsilon_1$ and $\varepsilon_2$) the anatase phase shows a kind of shoulder at the main peak, which is not present in

the modeled spectra similar to the rutile phase. Thus, the mesoporous $TiO_y$ layer could be an amorphous or not perfectly stoichiometric rutile $TiO_2$ layer.

From the fit results of the two Tauc–Lorentz functions (see Figure 2c), the band gap energy for the $TiO_y$ material is 2.95 eV. Compared to the band gap energies of the rutile phase ($E_g$ = 3.04 eV) [33] and the anatase phase ($E_g$ = 3.23 eV) [34], the band gap energy of the $TiO_y$ material is generally lower but very close to the value of the rutile phase, which reinforces the assumption of an amorphous rutile $TiO_2$ layer. In addition, a film thickness of 133.1 nm and a porosity value of 46.8% were derived from the fit. The most important results (i.e., film thickness and porosity) are summarized in Table 1 and will be discussed in detail together with the MSA results.

## 3.2 Mesoporous $IrO_x$ film

The mesoporous $IrO_x$ film was synthesized as described in ref. [35] and calcined at 400 °C in a preheated muffle furnace for 5 min in air. The top view SEM image in Figure 3a shows an ordered pore structure at the outer surface area and the cross-sectional image (Figure 3b) reveals a film with a uniform film thickness.

Similar to the modeling of the $TiO_y$ layers, a model was used for the mesoporous $IrO_x$ layer consisting of a Si substrate (literature values) [30, 31], a native oxide layer (literature values) [32], and a-BEMA (Eq. (1)) [18], which in turn consists of the $IrO_x$ material (Drude–Lorentz parametrization [Eqs. (7) and (9)]) and a void for the mesopores (Figure 3c). A detailed description of the model can be found in ref. [35].

Modeling of both Ψ and Δ spectra (measured at AOIs between 55 and 75°, in 5° steps) show good agreement in this case as well (Figure 4a and b). Again, slightly higher deviations in the range around 5 eV are observed in the modeled Δ spectra (Figure 4b), but in this case the $D_{RMS}$ value is no more than 8.274.

The dielectric functions were fitted by a Drude–Lorentz parameterization since the $IrO_x$ material is a conducting metal oxide (Figure 4c). Besides the Drude function in the low photon energy range (<2 eV), there is also a small absorption band at 1 eV represented by a Lorentz function. In addition, two absorption bands at 4 eV and at 7.6 eV are indicated by two Lorentz functions. The features in the

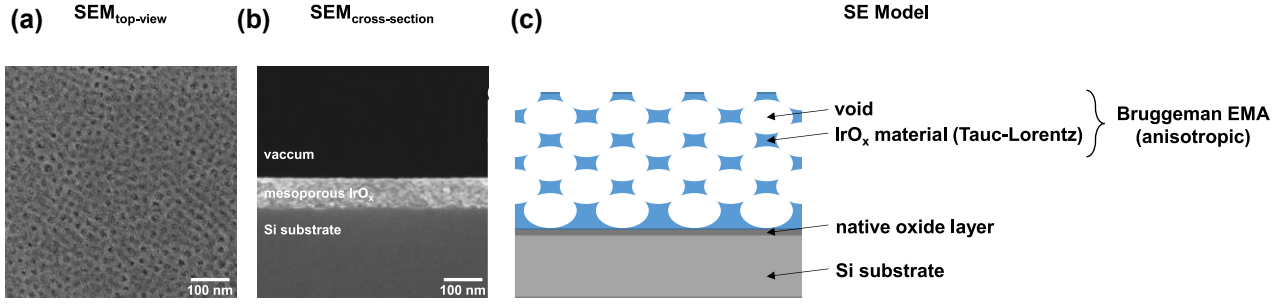


**Figure 3:** SEM images and spectroscopic ellipsometry model for the mesoporous $IrO_x$ film calcined in air at 400 °C for 5 min. a) Top-view SEM image indicating an ordered mesopore network at the outer surface area. b) SEM cross-section image shows a uniform film thickness of about 74 nm. c) Illustration of the model approach for ellipsometric analysis.

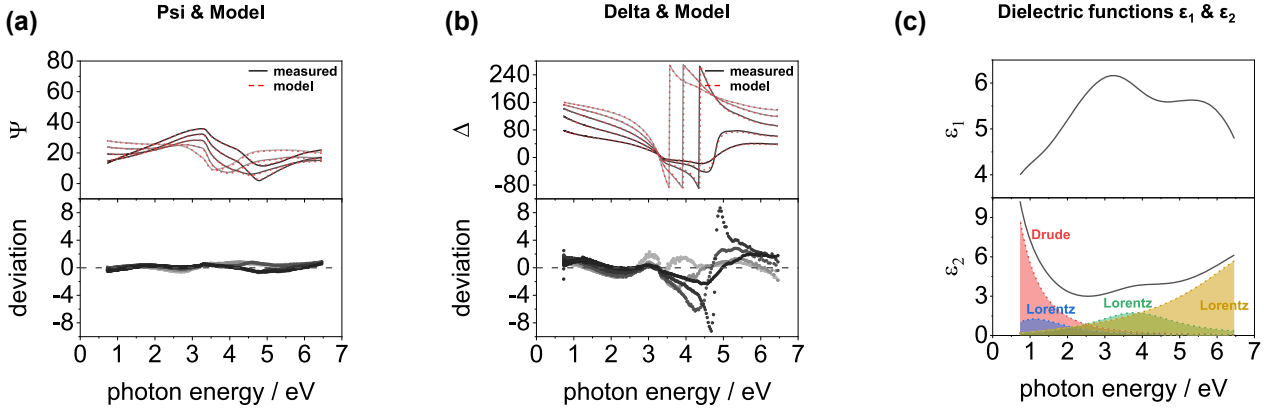


**Figure 4:** Ψ (a) and Δ (b) spectra with their fit results as well as the deviation between measured and modeled Ψ and Δ spectra. (c) Real ($\varepsilon_1$) and imaginary ($\varepsilon_2$) parts of the dielectric function of the mesoporous $IrO_x$ film calcined at 400 °C.

dielectric functions of the $IrO_x$ material can be attributed to free electron transitions and interband transitions. A more detailed description of these transitions can be found in refs. [35–37].

As a result of the fitting, parameters such as resistivity, film thickness and porosity can be derived. The resistivity value amount to $9.31 \cdot 10^{-4}$ Ω cm, the film thickness is 60.6 nm and a porosity value of 44.3% is obtained. Also in this case, the most important fitting results (film thickness and porosity) are summarized in Table 1 and will be discussed together with the derived results of the MSA.

## 3.3 Multi-sample analysis of $IrO_x$–$TiO_y$ films

Finally, with the two $TiO_y$ and $IrO_x$ models developed previously, the $IrO_x$–$TiO_y$ mixed oxide films with different compositions can be studied by spectroscopic ellipsometry. The $IrO_x$–$TiO_y$ mixed oxide films were also prepared via dip coating and synthesized in a slightly modified synthetic route as described in ref. [8]. The films were deposited on Si substrates and subsequently calcined in air at 400 °C for 10 min in a preheated muffle furnace.

Figure 5 shows top view and cross section SEM images of a mesoporous $IrO_x$–$TiO_y$ film with 30 $wt\%_{Ir}$ content in $Ir/TiO_2$, and the model used. The top view SEM image shows an ordered pore structure on the outer surface without any sign of phase separation. In the cross-sectional image, a uniform film thickness is observed.

A model consisting of a Si substrate (literature values) [30, 31], a native oxide layer (literature values) [32] and an a-BEMA (Eq. (1)) [18] for the mesoporous layer was used for modeling. The a-BEMA [18] layer contains the volume fractions of the material matrix and the void for the mesopores. The material matrix, in turn, was modeled with a Bruggeman EMA (Eq. (3)) containing the volume fractions of the dielectric functions of $TiO_y$ and $IrO_x$ material from the previously modeled pure metal oxide layers. Subsequently, $IrO_x$–$TiO_y$ films with an Ir-content between 0 $wt\%_{Ir}$ (pure $TiO_y$) and 100 $wt\%_{Ir}$ (pure $IrO_x$) were analyzed by MSA, where for each layer the film thickness, the volume fraction between the $TiO_y$ and $IrO_x$ material, the volume fraction of the void and the anisotropy in *z*-direction served as free parameters.

Figure 6 shows exemplary measurement raw data and the deviation between the measured and modeled Ψ and Δ spectra of the mesoporous $IrO_x$–$TiO_y$ film with 30 $wt\%_{Ir}$ content, as well as the changes of the dielectric functions as a function of the Ir-content within the layers.

The modeled values generally show good agreement with the measured Ψ and Δ spectra (AOIs 55–75°, 5° steps), although again there are larger deviations when modeling the Δ spectra (Figure 6a, b). The single $D_{RMS}$ value for the 30 $wt\%_{Ir}$ $IrO_x$–$TiO_y$ film is 48.161. However, the $D_{RMS}$ value of the MSA is only 44.922.

The dielectric functions show a systematic change with increasing Ir-content (Figure 6c). Thus, the 15 $wt\%_{Ir}$ $IrO_x$–$TiO_y$ film still shows a quite similar pattern of dielectric functions compared to the pure $TiO_y$ film. At 30 $wt\%_{Ir}$, an absorption feature slowly becomes visible in $\varepsilon_2$ in the low photon energy range (about 1 eV), which becomes more obvious with increasing Ir-content. This feature can be attributed to the increasing Ir-content and the resulting increase in free charge carriers (higher electrical conductivity). The typical absorption band of $TiO_y$ in the range of 3–4 eV ($\varepsilon_1$) and 4–5 eV ($\varepsilon_2$) also decreases significantly with increasing Ir-content.

The derived material parameters layer thickness, the volume fraction of void (porosity) and the volume fraction of $IrO_x$ (converted to $wt\%_{Ir}$) are shown in Figure 7.

The derived film thickness (Figure 7a) shows a film thickness around 140 nm (130–150 nm) for the films from

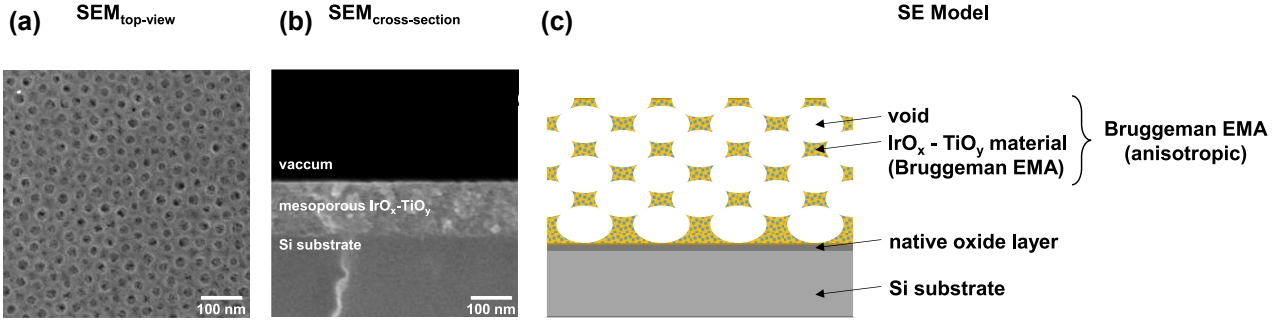


**Figure 5:** SEM micrographs of a mesoporous $IrO_x$–$TiO_y$ film with 30 $wt\%_{Ir}$ calcined in air at 400 °C for 10 min and the model approach for ellipsmetric analysis of the mesoporous $IrO_x$–$TiO_y$ films with different Ir-contents.
a) Top-view SEM image of the outer surface area with ordered mesopores. b) Cross-sectional SEM image of a uniform film thickness of about 135 nm. c) Illustraion of the ellipsometric model.

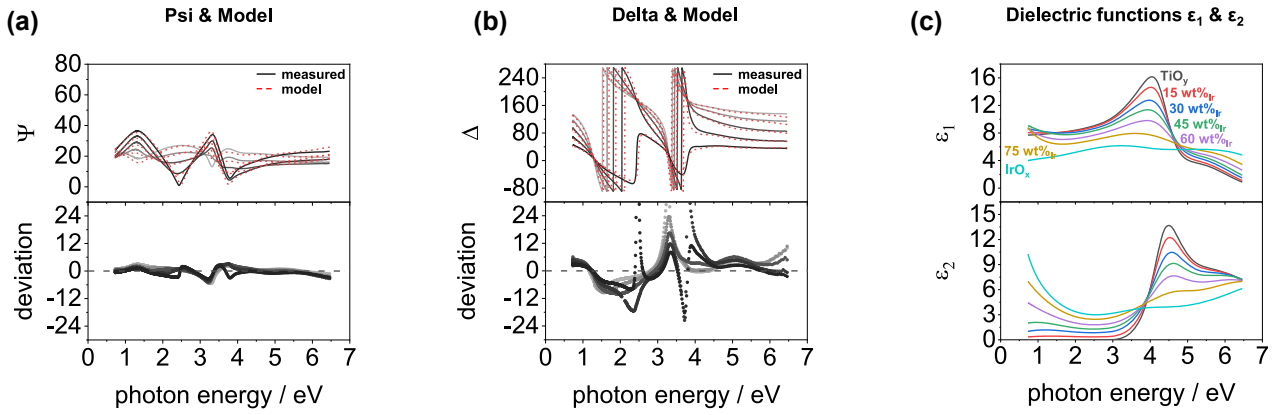


**Figure 6:** Ψ (a) and Δ (b) spectra and deviation between measured and modeled spectra of a mesoporous $IrO_x$–$TiO_y$ film with 30 $wt\%_{Ir}$. (c) Real ($\varepsilon_1$) and imaginary ($\varepsilon_2$) parts of the dielectric functions of mesoporous $IrO_x$–$TiO_y$ films with Ir-contents between 0 $wt_{Ir}$ ($TiO_y$) and 100 $wt_{Ir}$ ($IrO_x$).

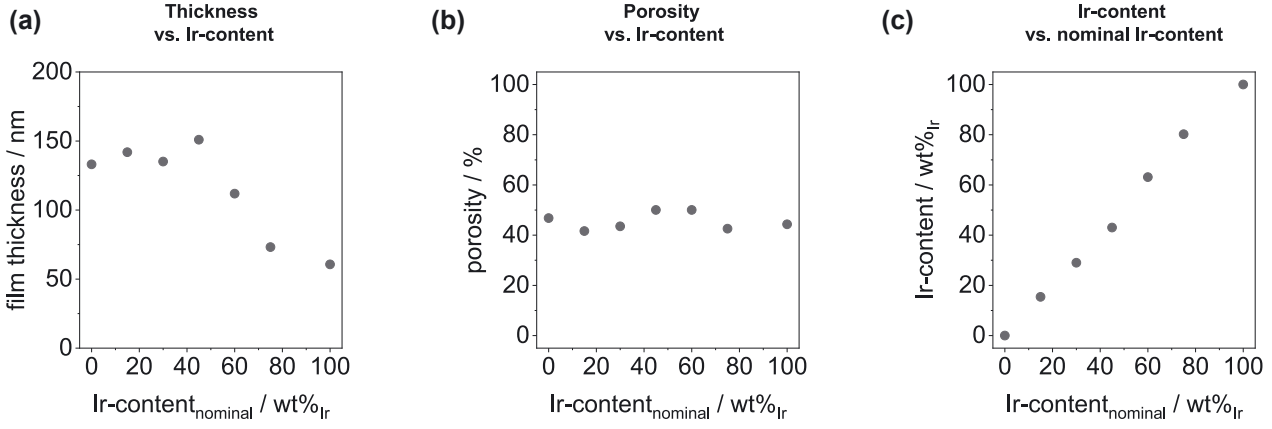


**Figure 7:** Results of ellipsometric modeling of mesoporous $IrO_x$–$TiO_y$ films with Ir-contents between 0 $wt_{Ir}$ ($TiO_y$) and 100 $wt_{Ir}$ ($IrO_x$). a) Film thickness versus the nominal Ir-content. b) Porosity and c) Ir-content as a function of the nominal Ir-content.

0 $wt\%_{Ir}$ to 45 $wt\%_{Ir}$, which decreases at higher Ir-content (>45 $wt\%_{Ir}$). All films were deposited on the Si substrates under the same conditions (25 °C ambient temperature, coating solution temperature of 40 °C, 40% relative humidity) and constant withdrawal rate of 200 mm $min^{-1}$. The differences in film thickness can therefore be attributed to the composition of the dip coating solution. We attribute this effect to changes in the viscosity of the solutions which leads to a variation of the amount of the amount of the solution coated on the substrate at constant withdrawal rate.

The derived volume fractions of the voids show a relatively constant value at about 45% over the entire variation of the films (Figure 7b). This is in good agreement with similarly synthesized mesoporous films of the types $TiO_y$, $IrO_x$ or their mixtures. It is also in good agreement with the fact that the same amount of template polymer was used for the different film syntheses and thus the porosity should be almost the same for all films.

The $IrO_x$ volume fractions converted to $wt\%_{Ir}$ (Ir in $Ir/TiO_2$) also show good agreement compared to the nominal Ir fraction used during synthesis (Figure 7c). Thus, the analysis shows a constant increase of the Ir-content with increasing amount of the Ir precursor used.

## 3.4 Validation of MSA fit results

Since spectroscopic ellipsometry (SE) is an indirect method, the results of the material parameters are strongly dependent on the quality of the optical model. In order to get an indication of the accuracy of the derived results, they are validated with complementary analytical methods. For this purpose, environmental ellipsometric porosimetry (EEP) was used to validate the porosity, SEM for the film thickness and EPMA for the Ir-content. Figure 8 shows the parity plots for layer thickness (SE versus SEM), porosity (SE versus EEP) and Ir-content

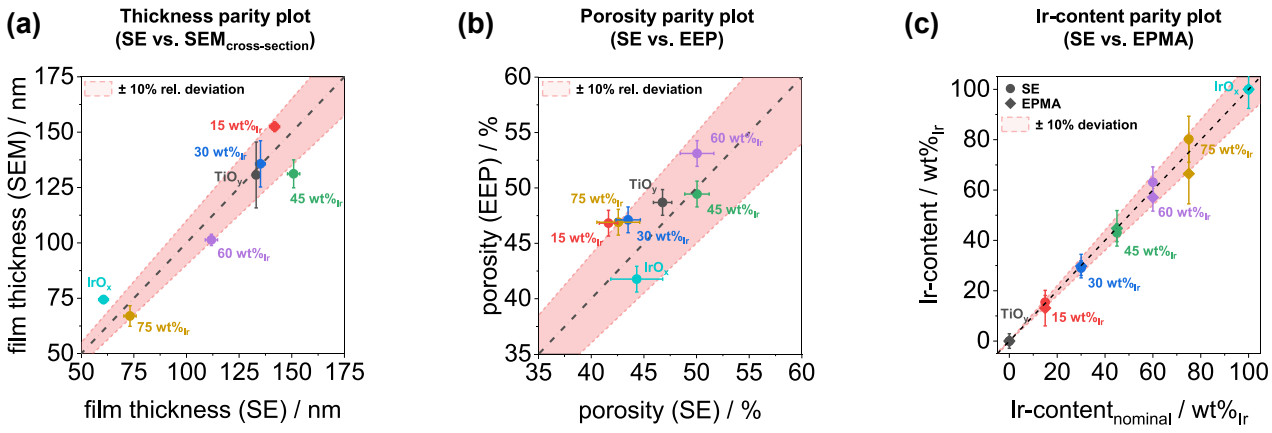


**Figure 8:** Validation of the fit results from spectroscopic ellipsometry modeling with complemantary analytic methods.
a) Parity plot of the film thickness from SEM cross-section images and SE modeling. b) Porosity values from EEP measurements versus SE porosity values. c) Ir-content from SE and EPMA as a function of the nominal Ir-content.

(SE versus EPMA versus nominal). The deviations of the ellipsometric methods (SE and EEP) were obtained by a sensitivity analysis for the respective parameter (i.e., layer thickness, porosity and Ir content), which is described in detail by Rosu et al. in ref. [27]. The deviations of the film thickness obtained by SEM cross-sectional images were determined by the standard deviation of several measurements along the fracture edge. For EPMA, the deviations were also determined by the standard deviations of the measured net peak X-ray intensities of interest.

The obtained film thicknesses from SE and SEM provide similar values in a range less than 15 nm and similar trends (Figure 8a). It should be noted that the exact same location could not be measured between the two methods. However, previous homogeneity analyses on $IrO_x$ films show that inhomogeneity contributes only negligible amounts to the result uncertainties [35]. Thus, the analysis using the ellipsometric model approach shows a good agreement for the film thickness for all measured samples in the range between 0 $wt\%_{Ir}$ and 100 $wt\%_{Ir}$ and all values are in the range of a relative deviation of about 10%.

EEP measurements are an accurate method for determining the porosity of thin films [38–40]. The porosity values of the EEP adsorption isotherms were determined using the same models as those of the SE analysis. The porosity values of the two methods agree to less than 10% (Figure 8b), which shows a good agreement of the measurement results of the two methods and also in this case the values are in the range of relative deviation of 10%. Comparable results on similar mesoporous layers are also reported in the literature [27, 29, 35].

The comparison of the Ir-content is performed with EPMA. In this analysis, X-ray intensities of interest are measured at different accelerating voltages using energy dispersive X-ray spectroscopy (EDS), normalized to electron probe current and lifetime and quantified using defined standards of each element. A detailed description of this approach can be found in refs. [17, 29, 35]. Both methods, SE and EPMA, provide a very good agreement with the material contents nominally used in the synthesis, which show a relative deviation of less than about 10% of the derived values (Figure 8c). It should be also noted that the SE modeling shows a slightly better agreement than EPMA at a higher Ir-content of 75 $wt\%_{Ir}$. However, all values of the two methods are within their deviations.

## 4 Conclusion and outlook

In this study, we have shown that parameters like film thickness, porosity, and chemical composition of complex thin mesoporous mixed metal oxide films of the iridium oxide-titanium oxide type are accessible to spectroscopic ellipsometric measurements. The modeling approach provides changes in optical properties as a function of material composition as well as material properties such as film thickness, porosity and Ir-content. The derived results from SE agree well with the values obtained by the complementary techniques SEM, EPMA and EEP.

The analytical approach described here also offers the possibility of correlating electrochemical activity properties with optical material parameters in future analyses. The relationship of the dielectric function to the energy loss function can contribute to a better understanding of the structure–activity relationship. In addition, spectroscopic ellipsometry, through its fast and vacuum-free analysis, offers the possibility to study

electrochemical reactions *in-situ* and/or operando under more realistic conditions, allowing a deeper understanding of catalytic systems.

**Author contributions:** All the authors have accepted responsibility for the entire content of this submitted manuscript and approved submission.

**Research funding:** Andreas Hertwig and René Sachse acknowledge generous funding from the project ATMOC (20IND04, Traceable metrology of soft X-ray to IR optical constants and nanofilms for advanced manufacturing). This project has received funding from the EMPIR programme co-financed by the Participating States and from the European Union's Horizon 2020 research and innovation programme. Ralph Kraehnert acknowledges generous funding of the DFG via SPP2080 (406695057) and of BMBF project ATO–KAT (03EK3052A).

**Conflict of interest statement:** The authors declare no conflicts of interest regarding this article.

## References

[1] E. Ortel, T. Reier, P. Strasser, and R. Kraehnert, "Mesoporous $IrO_2$ films templated by PEO–PB–PEO block-copolymers: self-assembly, crystallization behavior, and electrocatalytic performance," *Chem. Mater.*, vol. 23, pp. 3201–3209, 2011.

[2] M. Bernicke, E. Ortel, T. Reier, et al., "Iridium oxide coatings with templated porosity as highly active oxygen evolution catalysts: structure-activity relationships," *ChemSusChem*, vol. 8, pp. 1908–1915, 2015.

[3] J. P. Hughes, J. Clipsham, H. Chavushoglu, S. J. Rowley-Neale, and C. E. Banks, "Polymer electrolyte electrolysis: a review of the activity and stability of non-precious metal hydrogen evolution reaction and oxygen evolution reaction catalysts," *Renew. Sustain. Energy Rev.*, vol. 139, p. 110709, 2021.

[4] M. Huynh, C. Shi, S. J. L. Billinge, and D. G. Nocera, "Nature of activated manganese oxide for oxygen evolution," *J. Am. Chem. Soc.*, vol. 137, pp. 14887–14904, 2015.

[5] E. Willinger, C. Massué, R. Schlögl, and M. G. Willinger, "Identifying key structural features of IrOx water splitting catalysts," *J. Am. Chem. Soc.*, vol. 139, pp. 12093–12101, 2017.

[6] E. Oakton, D. Lebedev, A. Fedorov, et al., "A simple one-pot Adams method route to conductive high surface area $IrO_2$–$TiO_2$ materials," *New J. Chem.*, vol. 40, pp. 1834–1838, 2016.

[7] E. Oakton, D. Lebedev, M. Povia, et al., "$IrO_2$-$TiO_2$: a high-surface-area, active, and stable electrocatalyst for the oxygen evolution reaction," *ACS Catal.*, vol. 7, pp. 2346–2352, 2017.

[8] M. Bernicke, D. Bernsmeier, B. Paul, et al., "Tailored mesoporous $Ir/TiO_x$: identification of structure-activity relationships for an efficient oxygen evolution reaction," *J. Catal.*, vol. 376, pp. 209–218, 2019.

[9] D. Bernsmeier, M. Bernicke, R. Schmack, et al., "Oxygen evolution catalysts based on Ir–Ti mixed oxides with templated mesopore structure: impact of Ir on activity and conductivity," *ChemSusChem*, vol. 11, pp. 2367–2374, 2018.

[10] P. Jovanovič, N. Hodnik, F. Ruiz-Zepeda, et al., "Electrochemical dissolution of iridium and iridium oxide particles in acidic media: transmission electron microscopy, electrochemical flow cell coupled to inductively coupled plasma mass spectrometry, and X-ray absorption spectroscopy study," *J. Am. Chem. Soc.*, vol. 139, pp. 12837–12846, 2017.

[11] H. Fujiwara, *Spectroscopic Ellipsometry: Principles and Applications*, Chichester, West Sussex, John Wiley & Sons, 2007.

[12] A. Röseler, *Infrared Spectroscopic Ellipsometry*, Berlin, Akademie-Verlag, 1990.

[13] N. Krins, J. D. Bass, D. Grosso, et al., "$NbVO_5$ mesoporous thin films by evaporation induced micelles packing: pore size dependence of the mechanical stability upon thermal treatment and Li insertion/extraction," *Chem. Mater.*, vol. 23, pp. 4124–4131, 2011.

[14] R. A. May, L. Kondrachova, B. P. Hahn, and K. J. Stevenson, "Optical constants of electrodeposited mixed molybdenum–tungsten oxide films determined by variable-angle spectroscopic ellipsometry," *J. Phys. Chem. C*, vol. 111, pp. 18251–18257, 2007.

[15] O. Buiu, W. Davey, Y. Lu, I. Z. Mitrovic, and S. Hall, "Ellipsometric analysis of mixed metal oxides thin films," *Thin Solid Films*, vol. 517, pp. 453–455, 2008.

[16] E. Ortel, A. Fischer, L. Chuenchom, et al., "New triblock copolymer templates, PEO–PB–PEO, for the synthesis of titania films with controlled mesopore size, wall thickness, and bimodal porosity," *Small*, vol. 8, pp. 298–309, 2012.

[17] J.-L. Pouchou, "X-ray microanalysis of thin surface films and coatings," *Microchim. Acta*, vol. 138, pp. 133–152, 2002.

[18] D. Schmidt and M. Schubert, "Anisotropic Bruggeman effective medium approaches for slanted columnar thin films," *J. Appl. Phys.*, vol. 114, 2013, Art no. 083510.

[19] H. Tompkins and E. A. Irene, *Handbook of Ellipsometry*, Norwich, New York, William Andrew Publishing, 2005.

[20] B. von Blanckenhagen, D. Tonova, and J. Ullmann, "Application of the Tauc-Lorentz formulation to the interband absorption of optical coating materials," *Appl. Opt.*, vol. 41, pp. 3137–3141, 2002.

[21] G. E. Jellison Jr. and F. A. Modine, "Parameterization of the optical functions of amorphous materials in the interband region," *Appl. Phys. Lett.*, vol. 69, pp. 371–373, 1996.

[22] J. Tauc, R. Grigorovici, and A. Vancu, "Optical properties and electronic structure of amorphous germanium," *Phys. Status Solidi*, vol. 15, pp. 627–637, 1966.

[23] P. Drude, "Optische eigenschaften und elektronentheorie," *Ann. Phys.*, vol. 319, pp. 677–725, 1904.

[24] A. Sommerfeld and H. Bethe, *Elektronentheorie der Metalle*, Berlin Heidelberg, Springer-Verlag, 2013.

[25] T. E. Tiwald, D. W. Thompson, J. A. Woollam, W. Paulson, and R. Hance, "Application of IR variable angle spectroscopic ellipsometry to the determination of free carrier concentration depth profiles," *Thin Solid Films*, vol. 313–314, pp. 661–666, 1998.

[26] F. Wooten, Ed., "Absorption and dispersion," in *Optical Properties of Solids*, New York and London, Academic Press, 1972, chapter 3, pp. 42–84.

[27] D.-M. Rosu, E. Ortel, V.-D. Hodoroaba, R. Kraehnert, and A. Hertwig, "Ellipsometric porosimetry on pore-controlled $TiO_2$ layers," *Appl. Surf. Sci.*, vol. 421, pp. 487–493, 2017.

[28] E. Ortel, I. Häusler, W. Österle, et al., "In-depth structural and chemical characterization of engineered $TiO_2$ films," *Surf. Interface Anal.*, vol. 48, pp. 664–669, 2016.

[29] E. Ortel, A. Hertwig, D. Berger, et al., "New approach on quantification of porosity of thin films via electron-excited x-ray spectra," *Anal. Chem.*, vol. 88, pp. 7083–7090, 2016.
[30] C. M. Herzinger, B. Johs, W. A. McGahan, and W. Paulson, "A multi-sample, multi-wavelength, multi-angle investigation of the interface layer between silicon and thermally grown silicon dioxide," *Thin Solid Films*, vol. 313-314, pp. 281–285, 1998.
[31] C. M. Herzinger, B. Johs, W. A. McGahan, J. A. Woollam, and W. Paulson, "Ellipsometric determination of optical constants for silicon and thermally grown silicon dioxide via a multi-sample, multi-wavelength, multi-angle investigation," *J. Appl. Phys.*, vol. 83, pp. 3323–3336, 1998.
[32] M. Morita, T. Ohmi, E. Hasegawa, M. Kawakami, and M. Ohwada, "Growth of native oxide on a silicon surface," *J. Appl. Phys.*, vol. 68, pp. 1272–1281, 1990.
[33] T. E. Tiwald and M. Schubert, "Measurement of rutile TiO2 dielectric tensor from 0.148 to 33 um using generalized ellipsometry," in *Proc. SPIE 4103, Optical Diagnostic Methods for Inorganic Materials II*, L. M. Hanssen, Ed, vol. 4103, p. 11, 2000.
[34] G. E. Jellison, L. A. Boatner, J. D. Budai, B.-S. Jeong, and D. P. Norton, "Spectroscopic ellipsometry of thin film and bulk anatase ($TiO_2$)," *J. Appl. Phys.*, vol. 93, pp. 9537–9541, 2003.
[35] R. Sachse, M. Pflüger, J.-J. Velasco-Vélez, et al., "Assessing optical and electrical properties of highly active $IrO_x$ catalysts for the electrochemical oxygen evolution reaction via spectroscopic ellipsometry," *ACS Catal.*, vol. 10, pp. 14210–14223, 2020.
[36] A. K. Goel, G. Skorinko, and F. H. Pollak, "Optical properties of single-crystal rutile $RuO_2$ and $IrO_2$ in the range 0.5 to 9.5 eV," *Phys. Rev. B*, vol. 24, pp. 7342–7350, 1981.
[37] W. S. Choi, S. S. A. Seo, K. W. Kim, T. W. Noh, M. Y. Kim, and S. Shin, "Dielectric constants of Ir, Ru, Pt, and $IrO_2$: contributions from bound charges," *Phys. Rev. B*, vol. 74, p. 205117, 2006.
[38] M. R. Baklanov, K. P. Mogilnikov, V. G. Polovinkin, and F. N. Dultsev, "Determination of pore size distribution in thin films by ellipsometric porosimetry," *J. Vac. Sci. Technol. B*, vol. 18, pp. 1385–1391, 2000.
[39] C. Boissiere, D. Grosso, S. Lepoutre, L. Nicole, A. B. Bruneau, and C. Sanchez, "Porosity and mechanical properties of mesoporous thin films assessed by environmental ellipsometric porosimetry," *Langmuir*, vol. 21, pp. 12362–12371, 2005.
[40] A. Alvarez-Fernandez, B. Reid, M. J. Fornerod, A. Taylor, G. Divitini, and S. Guldin, "Structural characterization of mesoporous thin film architectures: a tutorial overview," *ACS Appl. Mater. Interfaces*, vol. 12, pp. 5195–5208, 2020.